

# Formation of Cavity-Polaritons via High-Order Van Hove Singularities

Igor Gianardi ,\* Michele Pini  and Francesco Piazza 

<sup>1</sup>*Max Planck Institute for the Physics of Complex Systems, 01187 Dresden, Germany*

<sup>2</sup>*Theoretical Physics III, Center for Electronic Correlations and Magnetism, Institute of Physics, University of Augsburg, 86135 Augsburg, Germany*

(Dated: September 22, 2025)

We consider polaritons formed by hybridizing particle-hole excitations of an insulating phase with a cavity photon at sub-gap frequencies, where absorption is suppressed. The strength of the hybridization is driven by the Van Hove singularity in the JDOS at the band gap: the stronger the singularity, the more a photon is hybridized with the interband transitions. In order to increase the singularity and thus the polariton hybridization without absorption, we propose to engineer a non-parabolic momentum dispersion of the bands around the gap in order to implement a high-order Van Hove singularity (HOVHS) in the JDOS. Ultracold atoms in tunable optical lattices are an ideal platform to engineer two-dimensional gapped phases with non-trivial band dispersions at the gap. Moreover, the intrinsic non-interacting nature of polarized fermionic atoms prevents the emergence of sub-gap excitations, which are common in solid-state systems and could otherwise spoil the absence of absorption below the gap. Our findings identify band-engineering at the gap edge as a promising route for polariton control with applications in quantum-nonlinear optics.

## I. INTRODUCTION

Polaritons are hybrid quasi-particles that blend matter and light properties [1]: an excitation of the electromagnetic field (i.e. a photon) can be converted into an excitation of the matter, and vice versa. For applications of polaritonics in quantum (nonlinear) optics [2] it is crucial that this back-and-forth exchange of excitations between the electromagnetic field and the matter takes place efficiently. This requires two main features: i) the coupling between light and matter is sufficiently strong, and ii) the absorption of photons from the matter has to be sufficiently small compared to the energy shift caused by the matter. The use of cavities for light confinement is useful for both i) and ii), as it increases the light-matter coupling as well as allows for tuning the photon spectrum with respect to the matter excitations.

In this work, we consider polaritons formed by the hybridization of cavity photons with interband transitions of an insulating material. This is promising since a photon tuned to the frequency range just below the band gap of the insulator does not suffer from absorption but can still experience a large energy shift through the hybridization with virtual interband particle-hole excitations.

Under these conditions, hybridization can be further increased by increasing the number of possible states between which the particle-hole can be excited, which is quantified by the joint density of states (JDOS) of the valence and conduction bands. In particular, the JDOS can even diverge at a Van Hove singularity (VHS). Since the divergence strength of VHSs increases as the system's dimensionality is reduced, one-dimensional systems are the most obvious candidates for the implementation of this mechanism. For such systems, the singularity consists of an inverse square-root divergence [3, 4]. Indeed,

the emergence of a cavity-polariton in presence of a VHS of the JDOS of an insulating phase was considered in the context of 1D nanowires [5].

In this work, we explore a promising alternative route to lowering the dimensionality to enhance the hybridization of Van Hove polaritons, namely the engineering of a non-parabolic momentum dispersion of the bands around the gap in order to implement a high-order Van Hove singularity (HOVHS) in the JDOS. HOVHSs have recently attracted interest in the solid-state community as a mean to modify transport and thermodynamical quantities, as well as enhance electron correlations [6–14]. In our case, we suggest instead to employ a HOVHS to increase the light-matter hybridization. In particular, we identify a specific band shape of a checkerboard lattice that gives rise to a new type of HOVHS, characterized by an inverse-square root divergence of the JDOS, further enhanced by a logarithm. To the best of our knowledge, this kind of HOVHS has not yet been reported in the existing solid-state-physics literature [8] and turns out to be useful for polaritonics.

We envision the cleanest implementation of high-order van Hove polaritons to be achievable with an ultracold gas of polarized fermionic atoms trapped in a checkerboard optical lattice and dispersively coupled to a single-mode optical cavity—a state-of-the-art setup [15]. The advantage of ultracold atoms over solid-state materials is the enhanced possibilities of band engineering, enabled by the tunability of the laser interference pattern [16–19]. Moreover, the form and strength of the light-matter coupling has been shown to be widely controllable [15], such that a non-zero coupling can be engineered for the relevant energies at which the HOVHS is present. Finally and probably most crucially, in ultracold atomic platforms sub-gap excitations, that would introduce absorption and spoil the VHS, are typically absent. Optical lattices are namely rigid and impurity-free, and the interatomic interactions can be tuned to zero e.g. using polar-

\* [gianardi@pks.mpg.de](mailto:gianardi@pks.mpg.de)

ized fermionic atoms. Indeed, while our description applies in principle also to solid-state platforms exhibiting strong VHSs in the JDOS, in most practical realizations the requirement of absence of absorption in the region below the band gap is typically more difficult to obtain than in ultracold atom platforms. This is due to the presence of electron-electron interactions or additional degrees of freedom such as phonons. In experiments, the failure to observe signatures of the VHS has been for instance attributed to excitons – observed in nanowires [20, 21], carbon nanotubes [22], conjugated polymers [23, 24], or bilayer graphene [25] – or more exotic types of excitations, as found in Blue-Bronzes [26]. Still, positive signatures of a VHS in a 2D topological insulator have been recently identified [27]. The paper is structured as follows. Section II presents our main results, showing how a novel 2D HOVHS can strongly enhance the hybridization of Van Hove polaritons. In Section III, we show the general mechanism behind the emergence of this class of polaritons. The nature of the HOVHS is further examined in Section IV, and its implementation with ultracold atoms is discussed in Section V. Throughout the paper, we set the reduced Planck constant  $\hbar$  to unity.

## II. KEY RESULTS

The scenario considered here is illustrated in Fig. 1. Photons confined within a cavity are coupled to the excitations of a crystalline material [see panel (a)]. These excitations have the band structure depicted in panel (b). As explained in the introduction, in order to maximize energy shifts by keeping the absorption negligible, we consider the case where the density of states associated with the material's bands is large above a gap of size  $E_g$  and vanishes immediately below it, as shown for example by the blue solid curve in panel (c) of Fig. 1. Therefore, a photon with frequency  $\omega \lesssim E_g$  interacting with particle-hole excitations with a coupling strength  $g$ , simultaneously experiences no absorption (as it cannot excite a particle into the conduction band) and a finite energy shift due to the hybridization with the virtual excitations. As anticipated in the introduction, in order to increase the energy shift experienced by the photon without increasing the absorption, we consider to increase the density of states—referred to in the context of interband transitions as the JDOS—of the excitations in the material. Instead of reducing the dimensionality of the latter, we propose to tailor the shape of the bands around the gap to increase the order of the VHS [4] in the JDOS, implementing a HOVHS. With this goal in mind, we identify a band-insulating phase on a checkerboard lattice, which gives rise to a new type of HOVHS, corresponding to a  $\log(\omega - E_g)/\sqrt{\omega - E_g}$  divergence in the JDOS at the band gap [see Fig. 1(c)]. This HOVHS is generated from the dispersion of the bands near the M point, which is quartic along the  $\Gamma$ M direction within the Brillouin Zone (BZ), and remains flat along the edges of

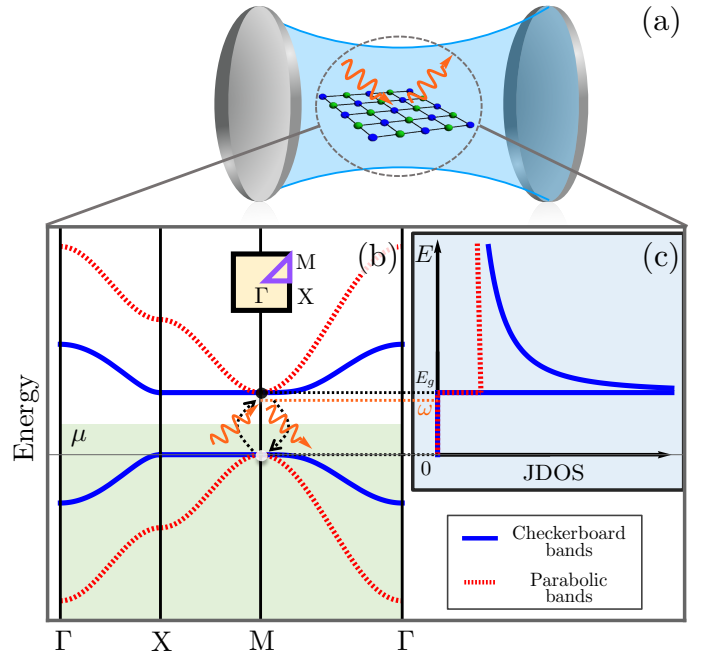


FIG. 1. Schematic illustration of the polariton formation mechanism at the gap edge of an insulator with engineered band dispersion. (a) Sketch of the system in real space: a material with a checkerboard lattice embedded in an optical cavity. (b) Energy bands of the checkerboard material (blue continuous line) compared to those of a standard parabolic insulator (red dotted line). The former shows near the M point a quartic dispersion along the  $\Gamma$ M direction within the BZ and flat bands along the BZ edges. The chemical potential is chosen so that the valence band is completely filled (green shaded region) and the conduction band is empty (white region), in order to have an insulating phase. Slightly below the band gap energy ( $\omega \lesssim E_g$ ), cavity photons (orange wavy arrows) hybridize with interband particle-hole excitations (black dashed arrows and circles). (c) Joint Density of States (JDOS) for both insulators. The parabolic bands case shows an ordinary step-like Van Hove singularity at the gap, while the engineered checkerboard bands one features a high-order Van Hove singularity.

the BZ, as illustrated in panel (b) of Fig. 1 (blue solid line). This deviates from the standard 2D parabolic case (red dashed line), which instead presents only an ordinary step-like VHS in the JDOS at the gap.

The formation of polaritons in this setting is shown in Fig. 2, where the photon spectral function  $A(\omega)$  (defined in Section III) is plotted as a function of the photon frequency  $\omega$  and the coupling strength  $g$ . Here, the cavity frequency  $\omega_0$  is set to be resonant with interband transitions at the band gap  $E_g$  in order to maximize the hybridization. When the photon has enough energy to excite the particle-hole continuum above the gap ( $\omega > E_g$ ), the spectral function shows a broadened polariton branch dominated by absorption processes. For photon frequencies below the gap ( $\omega < E_g$ ), the spectral function exhibits instead a very narrow, i.e. long-lived polaritonic

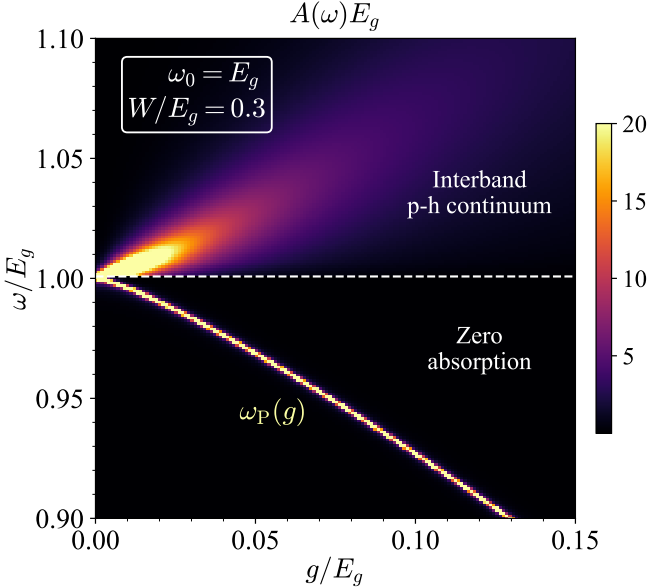


FIG. 2. Photon spectral function  $A(\omega)$  as a function of photon energy  $\omega$  and coupling strength  $g$ , with the cavity frequency  $\omega_0$  set equal to the band gap  $E_g$  of a checkerboard 2D lattice. The spectrum reveals two distinct regions. For  $\omega > E_g$ , the spectral function exhibits broadened features dominated by absorption processes. For  $\omega < E_g$ , a lower polaritonic branch emerges, characterized by zero absorption and a large energy shift.

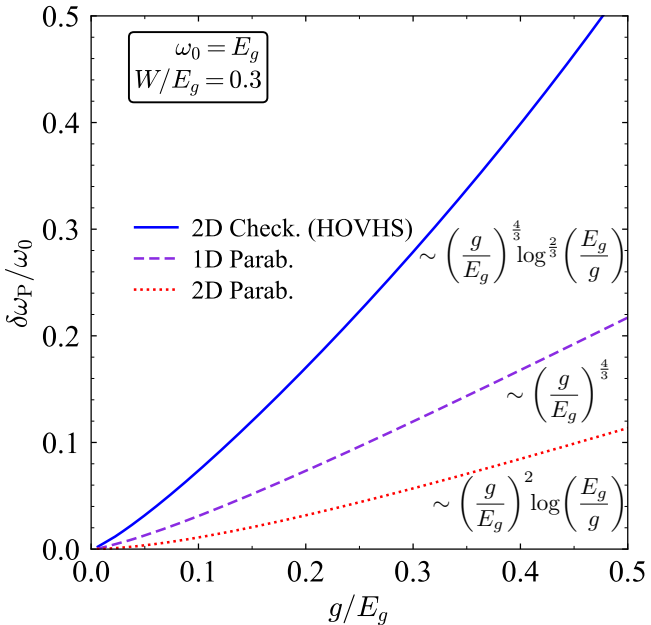


FIG. 3. The energy shift  $\delta\omega_P = \omega_0 - \omega_P$  of the lower polariton branch from the bare photon frequency  $\omega_0 = E_g$  is plotted as a function of the coupling strength  $g$  (in units of the bandwidth  $W$ ) for three cases of insulating band structures: 2D parabolic (red dotted line), 1D parabolic (purple dashed line), and 2D checkerboard (blue continuous line). The scaling laws as a function of  $g/E_g$  are reported next to the curves.

branch  $\omega_P(g)$  with a strong hybridization, evidenced by the strong bending of the branch away from the cavity frequency  $\omega_0 = E_g$  as the coupling strength  $g$  increases. The energy shift of the lower polaritonic branch is directly related to the order of the VHS: the stronger the divergence at the singularity, the greater the shift. This is further highlighted in Fig. 3, where the polariton energy shift  $\delta\omega_P$ , defined as the difference between the bare photon frequency  $\omega_0$  and the polaritonic branch  $\omega_P$ , is plotted for three different types of insulating band structures: 2D parabolic, 1D parabolic and 2D checkerboard. In the weak light-matter-coupling regime, the different kind of VHS in the three configurations implies a different scaling law of  $\delta\omega_P$  with the coupling  $g$ , written in Fig. 3 next to the curves. As we see, reducing the dimensionality from 2D to 1D increases the energy shift, as proposed in the context of nanowires in Ref. [5]. Notably, however, an even better scaling law is obtained for the 2D checkerboard case, highlighting band engineering of HOVHS in the JDOS as a more effective strategy than dimensionality reduction to enhance polariton hybridization.

### III. VAN HOVE POLARITONS

Without resorting to a specific lattice model for the matter, in this section we derive the role played by the JDOS of insulating bands on polariton formation, which allows us to discuss the effect of VHS. Employing a single-particle description for the insulating phase, the Hamiltonian in momentum space can be written as:

$$\hat{\mathcal{H}} = \hat{\mathcal{H}}_{\text{ph}} + \hat{\mathcal{H}}_M + \hat{\mathcal{H}}_{\text{int}} = \omega_0 \hat{a}^\dagger \hat{a} + \sum_{\lambda=\pm} \sum_{\mathbf{k} \in \text{BZ}} E_\lambda(\mathbf{k}) \hat{c}_{\lambda,\mathbf{k}}^\dagger \hat{c}_{\lambda,\mathbf{k}} + \sum_{\mathbf{k} \in \text{BZ}} \frac{g(\mathbf{k})}{\sqrt{N}} (\hat{a} + \hat{a}^\dagger) (\hat{c}_{+,\mathbf{k}}^\dagger \hat{c}_{-,\mathbf{k}} + \hat{c}_{-,\mathbf{k}}^\dagger \hat{c}_{+,\mathbf{k}}). \quad (1)$$

The first term represents free photons in a single cavity mode with frequency  $\omega_0$ , where  $\hat{a}^\dagger$  and  $\hat{a}$  are the photonic creation and annihilation operators. The second term accounts for fermions in the insulating phase, where  $E_\lambda(\mathbf{k})$  is the energy of the band  $\lambda$  (+ for conduction, - for valence) at momentum  $\mathbf{k}$  belonging to the 1<sup>st</sup> BZ, and  $\hat{c}_{\lambda,\mathbf{k}}^\dagger$  and  $\hat{c}_{\lambda,\mathbf{k}}$  are the fermionic creation and annihilation operators. The third term captures the light-matter interaction:  $g(\mathbf{k})$  quantifies the coupling between photons and vertical (i.e. zero-momentum transfer) interband excitations, scaled by the inverse square root of the number of unit cells,  $N$ . Fundamental to the description of cavity polaritons is the retarded photon propagator  $D_{\text{ph}}^R(t) = -i \theta(t) \langle [\hat{a}(t), \hat{a}^\dagger(0)] \rangle$ , with  $\theta(t)$  the Heaviside step function and  $\hat{a}(t) = e^{i\hat{\mathcal{H}}t} \hat{a} e^{-i\hat{\mathcal{H}}t}$  the photon annihilation operator in the Heisenberg picture. This propagator can be obtained through the Dyson equation

$$D_{\text{ph}}^R(\omega) = \left[ (D_{\text{ph},0}^R(\omega))^{-1} - \Sigma_{\text{ph}}^R(\omega) \right]^{-1}, \quad (2)$$

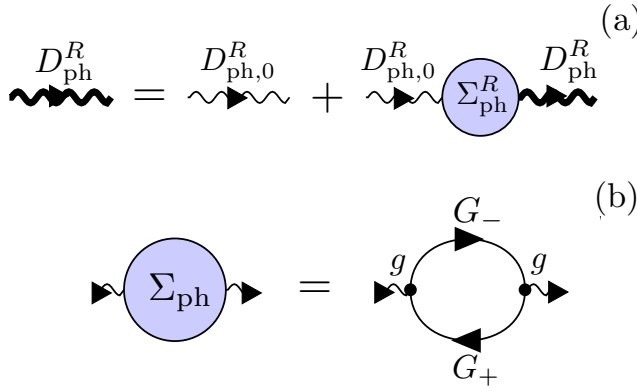


FIG. 4. Sketch of (a) the Dyson equation for the photon propagator (wiggly line) and (b) its self-energy due to the interaction with valence (−) and conduction (+) band electrons.

where  $D_{\text{ph},0}^R(\omega) = (\omega - \omega_0 + i0^+)^{-1}$  is the bare photon propagator, and  $\Sigma_{\text{ph}}^R(\omega)$  is the retarded photon self-energy. This equation is represented in terms of Feynman diagrams in Fig. 4(a). Once this quantity is calculated, the photon spectral function (represented in Fig. 2) follows directly from it:  $A(\omega) = -\frac{1}{\pi} \text{Im}[D_{\text{ph}}^R(\omega)]$ , and the lower polariton branch  $\omega_{\text{P}}$  (used in Fig. 3) is determined by the lower frequency pole of  $D_{\text{ph}}^R(\omega)$ , which can be obtained as the solution the implicit equation  $\omega - \omega_0 - \text{Re}[\Sigma_{\text{ph}}^R(\omega)] = 0$ . The self-energy can be computed perturbatively in the electron-photon interaction. This corresponds to the particle-hole bubble diagram represented in Fig. 4(b). The formal derivation of the above equations is detailed in Section A, where we obtain an effective action for the photon field by explicitly integrating out the fermionic degrees of freedom within the path-integral Matsubara formalism. The resulting expression for the self-energy is [28]

$$\Sigma_{\text{ph}}(\omega_{\nu}) = \frac{1}{\beta} \sum_{\mathbf{k}, \omega_n} g^2(\mathbf{k}) \left[ G_+(\mathbf{k}, \omega_n + \omega_{\nu}) G_-(\mathbf{k}, \omega_n) + G_-(\mathbf{k}, \omega_n + \omega_{\nu}) G_+(\mathbf{k}, \omega_n) \right], \quad (3)$$

where  $G_{\lambda}(\mathbf{k}, \omega_n) = [i\omega_n - E_{\lambda}(\mathbf{k})]^{-1}$  are the bare conduction/valence electron propagators,  $\beta = 1/k_{\text{B}}T$  with  $T$  being the temperature of the system, and  $\omega_n = (2n + 1)\pi T$  and  $\omega_{\nu} = 2\pi\nu T$  (with  $n, \nu$  integers) are bosonic and fermionic Matsubara frequencies, respectively. The retarded self-energy follows via analytic continuation  $\Sigma_{\text{ph}}^R(\omega) = \Sigma_{\text{ph}}(i\omega_{\nu} \rightarrow \omega + i0^+)$ . The retarded photon self-energy  $\Sigma_{\text{ph}}^R(\omega)$  can always be decomposed into an imaginary part, which sets the photon absorption rate (and thus the polariton damping appearing as a width of a peak in the spectral function), and a real part, which shifts the photon energy. In the zero-temperature

limit these components evaluate to

$$\text{Im}[\Sigma_{\text{ph}}^R(\omega)] = -\pi g^2 S [J(\omega) - J(-\omega)], \quad (4)$$

$$\text{Re}[\Sigma_{\text{ph}}^R(\omega)] = -2g^2 S \text{ P.V.} \int_0^{\infty} d\omega' \frac{\omega' J(\omega')}{\omega'^2 - \omega^2}, \quad (5)$$

where  $S$  is the surface area of the fermionic system and we introduced  $g \equiv g(\mathbf{k}^*)$ , with  $\mathbf{k}^*$  being the momentum critical point at which the interband energy splitting  $\delta E_{\mathbf{k}} = E_+(\mathbf{k}) - E_-(\mathbf{k})$  takes its global minimum  $E_g$ . If this minimum is degenerate, we select the point for which the largest number of momentum derivatives of  $\delta E_{\mathbf{k}}$  vanish. The rationale for this choice will become clear in Section IV. In Fig. 1, the point  $\mathbf{k}^*$  coincides with the M point,  $\mathbf{k}_M$ . Furthermore, we introduced the J DOS

$$J(\omega) = \frac{1}{S} \sum_{\mathbf{k} \in \text{BZ}} \delta(\omega - \delta E_{\mathbf{k}}), \quad (6)$$

which quantifies the density of states available for vertical inter-band transitions. Eqs. (4) and (5) explicitly highlight the importance of this quantity in characterizing the polariton.  $J(\omega)$  is typically vanishing below the band gap ( $\omega < E_g$ ) and presents a VHS above it ( $\omega \gtrsim E_g$ ). When the photon frequency  $\omega$  is tuned to a value just below the band gap  $E_g$  of the insulator, this automatically implies no absorption, since  $\text{Im}[\Sigma_{\text{ph}}^R(\omega < E_g)] \propto J(\omega < E_g) = 0$ . On the other hand, by performing the frequency integral in Eq. (5), it can be shown that a singularity in  $J(\omega)$  for  $\omega \gtrsim E_g$  leads to a singularity of equal or greater strength in  $\text{Re}[\Sigma_{\text{ph}}^R(\omega)]$  for  $\omega \lesssim E_g$  (an analytical proof is shown in Section C for the cases considered). This singularity in  $\text{Re}[\Sigma_{\text{ph}}^R(\omega)]$  is then directly reflected by the polariton energy, since the latter is determined by the implicit equation  $\delta\omega_{\text{P}} = -\text{Re}[\Sigma_{\text{ph}}^R(\omega = \omega_{\text{P}})]$ . This gives rise to the scaling laws of  $\delta\omega_{\text{P}}(g)$  represented in Fig. 3 for different cases.

As already evidenced in Section II, the strength of the VHS-effect on the self-energy depends on the dimensionality of the system and the local topology of the interband energy splitting  $\delta E_{\mathbf{k}}$  near  $\mathbf{k} = \mathbf{k}^*$ . We show this in Fig. 5, where we plot the real and imaginary part of  $\Sigma_{\text{ph}}^R(\omega)$  for three different types of insulating band structures: 2D parabolic with  $\delta E_{\mathbf{k}} \sim (\mathbf{k} - \mathbf{k}^*)^2$ , 1D parabolic with  $\delta E_{\mathbf{k}} \sim (k - k^*)^2$ , and 2D checkerboard with  $\delta E_{\mathbf{k}} \sim [(k_x - k_x^*)^2 - (k_y - k_y^*)^2]^2$  (see Section IV for a derivation of this dispersion within a tight-binding model on a checkerboard lattice). In the 2D parabolic case, the step-like behavior of  $\text{Im}[\Sigma_{\text{ph}}^R(\omega)]$  above gap results only in a logarithmic divergence in  $\text{Re}[\Sigma_{\text{ph}}^R(\omega)]$ . Reducing the dimensionality to 1D, but retaining parabolic bands, results in an enhancement of the above gap divergence of  $\text{Im}[\Sigma_{\text{ph}}^R(\omega)]$  to an inverse square root, which corresponds to divergence of equal strength in  $\text{Re}[\Sigma_{\text{ph}}^R(\omega)]$ . Finally, in the 2D checkerboard case, the engineered non-parabolic bands give rise to a novel type of HOVHS in the J DOS  $J(\omega)$ , which then appears in  $\text{Im}[\Sigma_{\text{ph}}^R(\omega)]$  and is reflected into  $\text{Re}[\Sigma_{\text{ph}}^R(\omega)]$ . The singularity features an

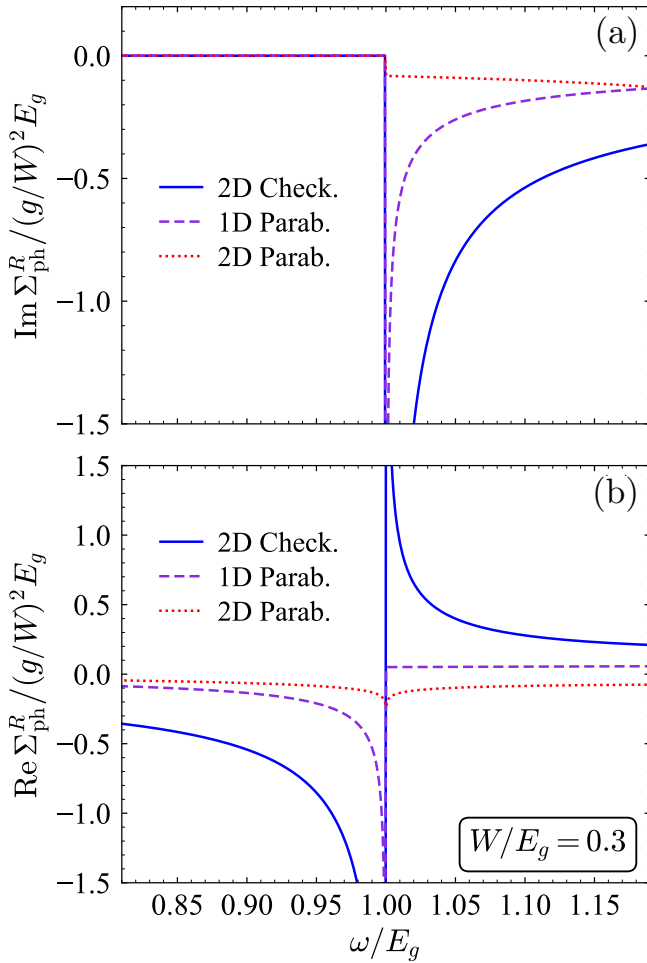


FIG. 5. Retarded photonic self-energy  $\Sigma_{\text{ph}}^R(\omega)$  near the band-gap energy  $E_g$  for three model insulators: 2D parabolic (red dotted), 1D parabolic (purple dashed), and 2D checkerboard (blue solid). (a) Imaginary part  $\text{Im}[\Sigma_{\text{ph}}^R(\omega)]$ . (b) Real part  $\text{Re}[\Sigma_{\text{ph}}^R(\omega)]$ .

inverse square-root divergence further enhanced by a logarithmic factor (see Sections B and C for the derivation):

$$J(\omega \rightarrow E_g^+) \sim \log \left( \frac{\omega - E_g}{E_g} \right) / \sqrt{\frac{\omega - E_g}{E_g}}, \quad (7)$$

$$\text{Re}[\Sigma_{\text{ph}}^R(\omega \rightarrow E_g^-)] \sim \log \left( \frac{E_g - \omega}{E_g} \right) / \sqrt{\frac{E_g - \omega}{E_g}}, \quad (8)$$

which is the strongest divergence of the three considered cases. The singular behaviors of the real and imaginary parts of the self-energy for the three insulating cases shown in Fig. 5 are summarized in Table I, along with the corresponding scaling laws for the polariton energy shift  $\delta\omega_{\text{P}}$  shown in Fig. 3.

	$\text{Im} \Sigma_{\text{ph}}^R(\omega \sim E_g^+)$	$\text{Re} \Sigma_{\text{ph}}^R(\omega \sim E_g^-)$	$\delta\omega_{\text{P}}$
<b>2D par.</b>	const.	$\log(1 - \omega/E_g)$	$-(\frac{g}{W})^2 \log(\frac{g}{W})$
<b>1D par.</b>	$\frac{1}{\sqrt{\omega/E_g - 1}}$	$\frac{1}{\sqrt{1 - \omega/E_g}}$	$-(\frac{g}{W})^{4/3}$
<b>2D ch.</b>	$-\frac{\log(\omega/E_g - 1)}{\sqrt{\omega/E_g - 1}}$	$\frac{\log(1 - \omega/E_g)}{\sqrt{1 - \omega/E_g}}$	$-(\frac{g}{W})^{4/3} \log^{2/3}(\frac{g}{W})$

TABLE I. Singular behavior of the imaginary and real parts of the retarded photon self-energies in the limit  $\omega \rightarrow E_g^{\pm}$ , and the corresponding polariton energy shifts  $\delta\omega_{\text{P}} = \omega_0 - \omega_{\text{P}}(g)$ . The results are shown for three insulating band structures: 2D parabolic, 1D parabolic, and 2D checkerboard lattice.

#### IV. ENGINEERED HOVHS WITH FERMIONS ON A CHECKERBOARD LATTICE

In this section, we show how a tight-binding model on a 2D checkerboard lattice can be used to engineer an insulating phase with a band dispersion around the gap featuring the desired HOVHS in the JDOS.

Let us consider a model of spinless fermions on a square lattice with a nearest-neighbor (NN) hopping of amplitude  $t$  and a staggered on-site potential of amplitude  $E_g$ . The corresponding Hamiltonian is given by:

$$\hat{\mathcal{H}}_M = -t \sum_{\mathbf{R}_j \in \Lambda_A} \sum_{l=1}^4 \left( \hat{c}_{\text{A}, \mathbf{R}_j}^{\dagger} \hat{c}_{\text{B}, \mathbf{R}_j + \delta_l} + \text{h.c.} \right) + \frac{E_g}{2} \left( \sum_{\mathbf{R}_j \in \Lambda_A} \hat{n}_{\text{A}, \mathbf{R}_j} - \sum_{\mathbf{R}_j \in \Lambda_B} \hat{n}_{\text{B}, \mathbf{R}_j} \right). \quad (9)$$

where fermionic creation (annihilation), and number operators  $\hat{c}_{\alpha, \mathbf{R}_j}^{\dagger}$  ( $\hat{c}_{\alpha, \mathbf{R}_j}$ ),  $\hat{n}_{\alpha, \mathbf{R}_j}$  have been introduced, respectively. These operators refer to fermions located at sites  $(\alpha, \mathbf{R}_j)$ , where the index  $j$  indicates the  $j$ -th site of the sublattice  $\{\Lambda_{\alpha}\}$ , and the index  $\alpha$  ( $= \text{A}, \text{B}$ ) specifies the sublattice. For terms describing hopping between NNs, the positions of the B-type sites are relative to the A-type sites, with the NN vectors  $\{\delta_1 = (a, 0); \delta_2 = (0, a); \delta_3 = -\delta_1; \delta_4 = -\delta_2\}$ , where  $a$  is the lattice spacing between A and B sites. This Hamiltonian can be easily diagonalized by performing a Fourier transformation  $\hat{c}_{\alpha, \mathbf{R}_j} = \frac{1}{\sqrt{N}} \sum_{\mathbf{k} \in \text{BZ}} e^{-i\mathbf{k} \cdot \mathbf{R}_j} \hat{c}_{\alpha, \mathbf{k}}$ , where  $N$  is the number of unit cells and the sum over  $\mathbf{k}$  runs over the 1<sup>st</sup> BZ shown in Fig. 6, and by applying the canonical basis change

$$\begin{aligned} \hat{c}_{-, \mathbf{k}} &= u_{\mathbf{k}} \hat{c}_{\text{A}, \mathbf{k}} - v_{\mathbf{k}} \hat{c}_{\text{B}, \mathbf{k}}, \\ \hat{c}_{+, \mathbf{k}} &= v_{\mathbf{k}} \hat{c}_{\text{A}, \mathbf{k}} + u_{\mathbf{k}} \hat{c}_{\text{B}, \mathbf{k}}, \end{aligned} \quad (10)$$

where  $u_{\mathbf{k}} = \sin \theta_{\mathbf{k}}/2$ ,  $v_{\mathbf{k}} = \cos \theta_{\mathbf{k}}/2$  and their ratio is given by  $\tan \theta_{\mathbf{k}} = \varepsilon_{\mathbf{k}}/E_g$  with  $\varepsilon_{\mathbf{k}} = -2t(\cos k_x a + \cos k_y a)$ . The diagonalized Hamiltonian is then:

$$\hat{\mathcal{H}}_M = \sum_{\lambda=\pm} \sum_{\mathbf{k} \in \text{BZ}} E_{\lambda}(\mathbf{k}) \hat{c}_{\lambda, \mathbf{k}}^{\dagger} \hat{c}_{\lambda, \mathbf{k}}, \quad (11)$$

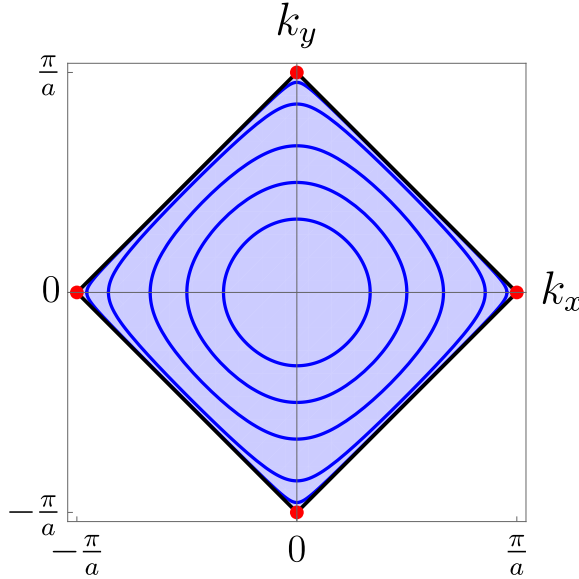


FIG. 6. Constant-energy contours within the diamond-shaped first BZ  $\mathcal{D}$  of the checkerboard lattice. Blue lines trace the contours, the black outline marks the BZ boundary, and the red dots indicate the M point and its symmetry-related images at the four vertices.

where the energy bands are given by

$$E_{\pm}(\mathbf{k}) = \pm \sqrt{\varepsilon_{\mathbf{k}}^2 + (E_g/2)^2}. \quad (12)$$

These energy bands were represented as solid blue lines in Fig. 1(b), and their contour lines within the BZ are represented in solid blue in Fig. 6. By Taylor expanding the dispersion near any of the four M points  $\mathbf{k}_M = \{(\pm\pi/a, 0), (0, \pm\pi/a)\}$ , highlighted in red in Fig. 6, we obtain

$$E_{\lambda}(\mathbf{k}) \approx \lambda \left\{ \frac{E_g}{2} + \gamma a^4 \left[ (k_x - k_{M,x})^2 - (k_y - k_{M,y})^2 \right]^2 \right\}, \quad (13)$$

where  $\lambda = \pm$  and we defined  $\gamma = t^2/E_g$ . The fact that the Hessian matrix  $\partial_{k_i} \partial_{k_j} E_{\lambda}(\mathbf{k})$  vanishes identically at the M point makes the latter a critical point associated with a type-I HOVHS [7]. The scaling behavior of this singularity in the JDOS was presented in Eq. (7), and its full analytical derivation is provided in Section B. The divergence appears as the product of two contributions at the band gap energy: an inverse square root factor and a logarithmic factor. The origin of this behavior can be understood as follows. The BZ boundary, shown in black in Fig. 6, forms a rotated square whose edges are dispersion-flat and have zero group velocity, thereby constituting critical lines. These critical lines are responsible for the one dimensional inverse square root factor, whereas the additional logarithmic factor originates from the intersection of the critical lines at the square's M vertices. We note that a conventional 2D VHS, which shows a purely logarithmic divergence, arises from a quadratic

saddle point situated at the crossing of two non-critical iso-energy lines [29]. To the best of our knowledge, the singularity reported here has not been previously documented, because it is associated with a local minimum of the dispersion and has a infinite codimension (see Section VII of [8]), while current VHS classifications have thus far addressed only saddle-point scenarios with finite codimension [8].

## V. IMPLEMENTATION: ULTRACOLD ATOMS IN OPTICAL LATTICES COUPLED TO A SINGLE MODE CAVITY

In this section, we present a physical implementation of the Hamiltonian of Eq. (9) with a system of fermionic ultracold atoms in a checkerboard optical lattice. We then propose a cavity-QED setup where the full light-matter Hamiltonian of Eq. (1) can be implemented.

### A. Matter

Let us consider an ultracold gas of spin-polarized fermionic atoms of mass  $m$ . We assume the cloud to be strongly confined along the  $z$  axis, making the system effectively 2D, and trapped in the  $x - y$  plane by a periodic potential of the form

$$\mathcal{V}(\mathbf{r}) = -V_0 [\cos^2 k_L x + \cos^2 k_L y + 2 \cos \theta \cos k_L x \cos k_L y], \quad (14)$$

see Ref. [30] for a possible experimental implementation. This specific potential gives rise to a square optical lattice composed of two classes (A and B) of lattice sites with different well depths arranged on a checkerboard, as shown in Fig. 7(a). The phase  $\theta$  in Eq. (14) allows to adjust the relative depth of the potential wells at sites A and B. This system is described by the Hamiltonian  $\hat{\mathcal{H}}_M = \int d\mathbf{r} \hat{\psi}^\dagger \hat{H}_M \hat{\psi}$ , with  $\hat{\psi}(\mathbf{r})$  being the fermionic field operator that annihilates an atom at position  $\mathbf{r} = (x, y)$ , and  $\hat{H}_M = -(1/2m)\nabla^2 + \mathcal{V}(\mathbf{r})$  being the single-particle Hamiltonian density. Since the gas is spin-polarized, the two-body interactions between fermions are absent, making the single-particle description exact [31, 32]. We will now derive the Hamiltonian of the checkerboard insulator given in Eq. (9). We assume that the potential wells are deep enough to allow us to map the Hamiltonian  $\hat{\mathcal{H}}_M$  onto a tight-binding model on the discrete lattice corresponding to the potential minima. This approximation is implemented by expanding the field operator  $\hat{\psi}(\mathbf{r})$  on a basis  $\{f_{nj}(\mathbf{r})\}$  of functions localized around each minimum [33]

$$\hat{\psi}(\mathbf{r}) = \sum_j \sum_{\alpha=A,B} f_{\alpha,j}(\mathbf{r}) \hat{c}_{\alpha,j}, \quad (15)$$

where the fermionic operators  $\hat{c}_{\alpha,j}$  were defined in Section IV. In the presence of a double well in the unit

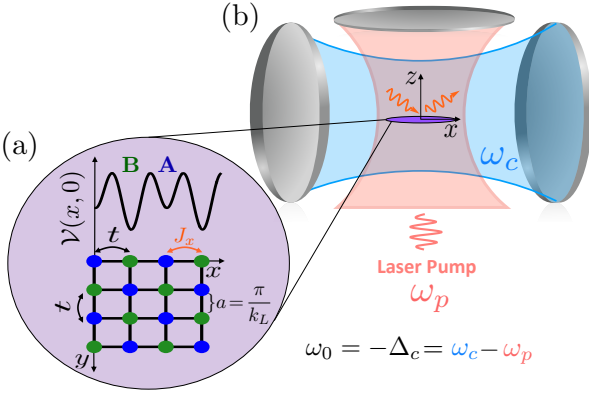


FIG. 7. (a) *Bottom*: checkerboard lattice in the  $x$ - $y$  plane with isotropic hopping  $t$  between sub-lattice sites  $A$  and  $B$ ; cavity photons couple to the fermions via cavity-assisted hopping along the  $x$  direction. *Top*: cut at  $y = 0$  of the optical potential  $\mathcal{V}(\mathbf{r})$  of Eq. (14). (b) A 2D Fermi gas, confined by the lattice of panel (a), is loaded into a linear standing-wave cavity of resonance frequency  $\omega_c$  whose axis lies along  $x$ . The atoms are driven by a transverse standing-wave pump laser of frequency  $\omega_p$  propagating along  $z$ . The transverse pump and intra-cavity lattices are shaded in blue and pink, respectively.

cell, the functions  $f_{\alpha,j}(\mathbf{r})$  have to be interpreted as the 2D-version of the generalized Wannier fuctions proposed by Modugno in Ref. [34]. In the following, we will restrict the analysis to the two lowest energy bands, in analogy with the single-band approximation for the Fermi–Hubbard model [35]. Then, within this approximation, the single-particle Hamiltonian can be written as:

$$\hat{\mathcal{H}}_M \approx \sum_{\alpha\alpha'=A,B} \sum_{jj'} \langle f_{\alpha,j} | \hat{H}_M | f_{\alpha',j'} \rangle \hat{c}_{\alpha,j}^\dagger \hat{c}_{\alpha',j'} \quad (16)$$

Here the expansion coefficients correspond to the on-site sublattice energies  $\epsilon_\alpha = \langle f_{\alpha,j} | \hat{H}_M | f_{\alpha,j} \rangle$ , and to minus the tunneling amplitudes between different subwells  $t_{\alpha\alpha'}^{jj'} = -\langle f_{\alpha,j} | \hat{H}_M | f_{\alpha',j'} \rangle$ . Under the tight-binding approximation [35] and absorbing into the chemical potential  $\mu$  all the elements proportional to the identity, the Hamiltonian in Eq. (16) can be mapped to the Hamiltonian in Eq. (9) with  $E_g = \epsilon_A - \epsilon_B$ .

## B. Coupling to Light

Let us now assume that the atomic cloud trapped in the optical lattice is loaded inside a single-mode linear standing-wave cavity with cavity axis aligned along  $x$  and resonance frequency  $\omega_c$ . The atoms are driven by a transverse standing-wave pump of frequency  $\omega_p$  with a detuning from the cavity frequency  $\Delta_c = \omega_p - \omega_c < 0$ . The pump is oriented along the  $z$  direction, i.e. orthogonally to both the cavity axis and to the plane in which the atoms are trapped, as sketched in Fig. 7(b). We

operate in the dispersive regime, where the detuning  $\Delta_a = \omega_p - \omega_a$  of the pump frequency with respect to the frequency  $\omega_a$  of an internal atomic transition is much larger than any other energy scale in the system. Under this condition, the atomic excited state can be adiabatically eliminated, and the dynamics of the atom–cavity system is governed by [15]

$$\begin{aligned} \hat{\mathcal{H}} = & -\Delta_c \hat{a}^\dagger \hat{a} \\ & + \int d\mathbf{r} \hat{\psi}^\dagger(\mathbf{r}) \left[ -\frac{\nabla^2}{2m} + \mathcal{V}(\mathbf{r}) \right. \\ & \left. + U(\mathbf{r}) \hat{a}^\dagger \hat{a} + \eta_{1D}(\mathbf{r}) (\hat{a}^\dagger + \hat{a}) \right] \hat{\psi}(\mathbf{r}) \end{aligned} \quad (17)$$

where the Hamiltonian is written directly in the  $z = 0$  plane where the atoms are confined.  $\mathcal{V}(\mathbf{r})$  is the 2D checkerboard potential of Eq. (14). The cavity mode generates an intracavity lattice  $U(\mathbf{r}) = U_0 \cos^2(q_c x)$ . The transverse pump creates a standing wave  $V(\mathbf{r}, z) = V_0 \cos^2(q_p z)$  that, at  $z = 0$ , reduces to the uniform offset  $V_0$ ; this constant simply renormalizes the chemical potential and is therefore omitted from the Hamiltonian. Interference between pump and cavity fields gives the position-dependent atom–photon coupling  $\eta(\mathbf{r}, z) = \eta_0 \cos(q_c x) \cos(q_p z)$ , which in the plane  $z = 0$  becomes the one-dimensional lattice  $\eta_{1D}(\mathbf{r}) = \eta_0 \cos(q_c x)$  that enters the Hamiltonian. The coupling strength  $\eta_0$  follows from the position-dependent Rabi frequency  $\Omega(\mathbf{r}, z) = \Omega_0 \cos(q_p z)$  and light–matter coupling  $\mathcal{G}(\mathbf{r}) = \mathcal{G}_0 \cos(q_c x)$ :  $V_0 = \Omega_0^2 / \Delta_a$ ,  $U_0 = \mathcal{G}_0^2 / \Delta_a$ , and  $\eta_0 = \Omega_0 \mathcal{G}_0 / \Delta_a$  [15]. Additionally we choose  $q_c = 2k_L$ , so that the periodicity of  $\eta(\mathbf{r})$  along  $x$  is twice the one of  $\mathcal{V}(\mathbf{r})$ .

To show that this system hosts HOVHS-polaritons, it is sufficient to map the Hamiltonian (17) onto the effective Hamiltonian (1). To this end, the matter sector has already been mapped in Sec. V A. Mapping the photonic part is straightforward once we identify the bare cavity frequency  $\omega_0$  with the negative detuning  $-\Delta_c > 0$ . The residual diamagnetic contribution merely produces a uniform dispersive shift and can be absorbed into a redefinition of the cavity detuning, as shown in Ref. [36]. The only term that still calls for an explicit treatment is the interaction vertex  $(\hat{a} + \hat{a}^\dagger) \int d\mathbf{r} \eta_{1D}(\mathbf{r}) \hat{\psi}^\dagger(\mathbf{r}) \hat{\psi}(\mathbf{r})$ , which needs to be mapped to  $\hat{\mathcal{H}}_{\text{int}}$  in Eq. (1). The choice  $q_c = 2k_L$  makes the periodic function  $\eta_{1D}(\mathbf{r})$  commensurate with the bipartite lattice, thereby allowing us to express  $\hat{\mathcal{H}}_{\text{int}}$  in the basis  $\{f_{nj}(\mathbf{r})\}$  of generalized Wannier functions [see Eq. (15)]:  $\hat{\mathcal{H}}_{\text{int}} = (\hat{a} + \hat{a}^\dagger) \sum_{\alpha\alpha'=A,B} \sum_{jj'} \langle f_{\alpha,j} | \hat{\eta}_{1D} | f_{\alpha',j'} \rangle \hat{c}_{\alpha,j}^\dagger \hat{c}_{\alpha',j'}$ . Neglecting hopping beyond nearest neighbors,  $\hat{\mathcal{H}}_{\text{int}}$  can be

further written as

$$\begin{aligned}\hat{\mathcal{H}}_{\text{int}} = & (\hat{a} + \hat{a}^\dagger) \sum_{l=1,3} J_x \sum_{\mathbf{R}_j \in \Lambda_A} (\hat{c}_{A,\mathbf{R}_j}^\dagger \hat{c}_{B,\mathbf{R}_j+\delta_l} + \text{h.c.}) \\ & + (\hat{a} + \hat{a}^\dagger) \sum_{l=2,4} J_y \sum_{\mathbf{R}_j \in \Lambda_A} (\hat{c}_{A,\mathbf{R}_j}^\dagger \hat{c}_{B,\mathbf{R}_j+\delta_l} + \text{h.c.}) \\ & + (\hat{a} + \hat{a}^\dagger) \sum_{\alpha=A,B} C_\alpha \sum_{\mathbf{R}_j \in \Lambda_\alpha} \hat{n}_{\alpha,\mathbf{R}_j},\end{aligned}\quad (18)$$

where we defined the sublattice-dependent density-coupling constants  $C_\alpha \equiv \langle f_{\alpha,j} | \hat{\eta}_{1D} | f_{\alpha,j} \rangle$  and the cavity-assisted hopping amplitudes  $J_x \equiv \langle f_{A,\mathbf{R}_j} | \hat{\eta}_{1D} | f_{B,\mathbf{R}_j+\delta_1} \rangle = \langle f_{A,\mathbf{R}_j} | \hat{\eta}_{1D} | f_{B,\mathbf{R}_j+\delta_3} \rangle$  and  $J_y \equiv \langle f_{A,\mathbf{R}_j} | \hat{\eta}_{1D} | f_{B,\mathbf{R}_j+\delta_2} \rangle = \langle f_{A,\mathbf{R}_j} | \hat{\eta}_{1D} | f_{B,\mathbf{R}_j+\delta_4} \rangle$ . Note that the equality of the cavity-assisted hopping amplitudes for the two pairs of displacement vectors oriented along the same axis,  $(\delta_1, \delta_3)$  along  $x$  and  $(\delta_2, \delta_4)$  along  $y$ , stems from the fact that  $\eta_{1D}(\mathbf{r}_\parallel)$  is invariant under reflections centered on the lattice sites. In the Bloch basis (10), the Hamiltonian  $\hat{\mathcal{H}}_{\text{int}}$  takes the form

$$\hat{\mathcal{H}}_{\text{int}} = (\hat{a} + \hat{a}^\dagger) \sum_{\lambda} \sum_{\mathbf{k} \in \text{RBZ}} g_{\lambda\lambda}(\mathbf{k}) \hat{c}_{\lambda,k}^\dagger \hat{c}_{\lambda',k}, \quad (19)$$

where we defined the intraband couplings  $g_{\lambda\lambda}(\mathbf{k}) = \bar{C} + \lambda \left( \frac{\delta C E_g / 2 + 2\epsilon_{\mathbf{k}} \xi_{\mathbf{k}}}{\sqrt{E_g^2 + 4\epsilon_{\mathbf{k}}^2}} \right)$  and the interband couplings  $g_{+-}(\mathbf{k}) = g_{-+}(\mathbf{k}) = \left( \frac{\delta C \epsilon_{\mathbf{k}} - \xi_{\mathbf{k}} E_g}{\sqrt{E_g^2 + 4\epsilon_{\mathbf{k}}^2}} \right)$  with  $\bar{C} = \frac{C_A + C_B}{2}$ ,  $\delta C = C_A - C_B$  and  $\xi_{\mathbf{k}} = -2J_x \cos k_x a - 2J_y \cos k_y a$ . We recall from Section IV that  $\epsilon_{\mathbf{k}} = -2t(\cos k_x a + \cos k_y a)$ . The mapping is complete once the interband coupling is identified as  $g(\mathbf{k}) = g_{+-}(\mathbf{k})$ . Intraband terms can be neglected as they do not contribute to the photonic self-energy due to the absence of quasi-momentum transfer in the interaction. Since  $\eta_{1D}(\mathbf{r})$  is uniform along the  $y$ -axis and the generalized Wannier functions are orthonormal [34], the cavity-assisted hopping amplitude in the  $y$ -direction,  $J_y$ , vanishes identically. As a result, the light-matter coupling at the HOVHS reads  $g(\mathbf{k}^*) = 2J_x$ . This anisotropy is crucial: were the hopping isotropic,  $J_x = J_y$ , the interband coupling would vanish at  $\mathbf{k}^*$ .

## VI. CONCLUSIONS

We have shown that band engineering of fermionic insulators coupled to cavity photons allows to enhance hybridization between light and matter via high-order Van-Hove singularities. By tuning the cavity resonance frequency just below the insulating gap, this leads to the formation of polaritons experiencing a strong energy shift without appreciable absorption. This approach provides an alternative to dimensionality reduction proposed in [5], that can lead to a better scaling law of the energy shift with the light-matter coupling.

In this work, we have focused on an ultracold atom implementation which is available in state-of-the-art setups. The main reason for this is the absence of lattice

excitation, impurities, and the possibility of tuning the atom-atom interactions to zero thereby removing further in-gap modes (like excitons) that would spoil the quality of the Van Hove singularity and its positive effect on the polariton properties.

In the future, a detailed investigation of a solid-state implementation of this mechanism seems important, also in view of the constant progress being made in the investigation of high-order Van Hove singularities especially in layered materials [7, 11–13]. From an experimental point of view, practical routes exist to suppress the excitonic effects that typically dominate the subgap region of these materials—for example, by engineering the surrounding dielectric environment [37, 38]. In this spirit, we would like to conclude by stressing a generic advantage of the polaritons discussed here, resulting from hybridization between photons and inter-band particle-hole excitations, and the well established exciton-polaritons [39]. This advantage is relevant for the purpose of (quantum) nonlinear optics and stems from the fact that, while exciton-polaritons inherit their nonlinearity from the residual exciton-exciton interactions (typically weak), the coupling between particle-hole excitations and photons is intrinsically non-linear: polaritons in this case will interact via the high-order polarization functions of the matter. The latter will also be enhanced by Van Hove singularities, as is the lowest order polarization function discussed here as the photon self-energy. This aspect will be the object of future investigation.

## Appendix A: Derivation of $\Sigma_{\text{ph}}^R(\omega)$

The aim of this section is to derive the photonic retarded self-energy  $\Sigma_{\text{ph}}^R(\omega)$ , whose imaginary and real parts are given in Eqs. (4) and (5). This quantity arises naturally within the construction of the photonic effective theory through the path integral formalism on the imaginary time-axis  $\tau \in [0, \beta]$ , with  $\beta$  the inverse temperature. The action corresponding to the Hamiltonian in Eq. (1) is quadratic in the fermionic fields, which can thus be integrated out exactly. The resulting effective action for the photons, decomposing the field into Matsubara components  $\alpha(\tau) = \frac{1}{\beta} \sum_{\omega_\nu} \alpha(\omega_\nu) e^{-i\omega_\nu \tau}$ , becomes [36]

$$\begin{aligned}\mathcal{S}_{\text{ph}}[\alpha, \alpha^*] = & \frac{1}{\beta} \sum_{\omega_\nu} (-i\omega_\nu + \omega_0) \alpha^*(\omega_\nu) \alpha(\omega_\nu) \\ & - \text{Tr}\{\log \mathcal{M}[\alpha, \alpha^*]\},\end{aligned}\quad (\text{A1})$$

where we defined the matrix

$$\mathcal{M}_{ab}[\alpha, \alpha^*] = -\mathcal{G}_{ab}^{-1} + \mathcal{A}_{ab}[\alpha, \alpha^*], \quad (\text{A2})$$

where the latin letters denote the full set of fermionic indices  $(\mathbf{k}, \omega_n, \lambda)$ , and the matrices  $\mathcal{G}_{ab}$  and  $\mathcal{A}_{ab}[\alpha, \alpha^*]$

are defined as

$$\mathcal{G}_{ab}^{-1} = G_{\lambda}^{-1}(\mathbf{k}, \omega_n) \delta_{\lambda, \lambda'} \delta_{\omega_n, \omega'_n} \delta_{\mathbf{k}, \mathbf{k}'} \quad (\text{A3})$$

$$\begin{aligned} \mathcal{A}_{ab}[\alpha, \alpha^*] &= g(\mathbf{k}) \frac{(1 - \delta_{\lambda, \lambda'})}{\sqrt{\beta}} \delta_{\omega_n, \omega'_n - \omega_n} \delta_{\mathbf{k}, \mathbf{k}'} \\ &\times (\alpha(\omega_n) + \alpha^*(-\omega_n)), \end{aligned} \quad (\text{A4})$$

with  $G_{\lambda}(\mathbf{k}, \omega_n) = [i\omega_n - E_{\lambda}(\mathbf{k})]^{-1}$  being the fermionic propagator and the chemical potential  $\mu$  was set to zero. In order to compute the photon self-energy used in the main text, we expand the logarithm up to second order  $\text{Tr}\{\log \mathcal{M}\} \approx \text{Tr}\{\log \mathcal{G}^{-1}\} + \text{Tr}\{\mathcal{G}\mathcal{A}\} - \frac{1}{2}\text{Tr}\{(\mathcal{G}\mathcal{A})^2\}$  to obtain the following effective action:

$$\mathcal{S}_{\text{ph}}[\alpha, \alpha^*] = -\frac{1}{2\beta} \sum_{\omega_n} (\alpha^*(\omega_n) \alpha(\omega_n)) \mathcal{D}_{\text{ph}}^{-1}(\omega_n) \begin{pmatrix} \alpha(\omega_n) \\ \alpha^*(\omega_n) \end{pmatrix}, \quad (\text{A5})$$

where the inverse cavity propagator reads:

$$\mathcal{D}_{\text{ph}}^{-1}(\omega_n) = \begin{pmatrix} i\omega_n - \omega_0 - \Sigma_{\text{ph}}(\omega_n) & -\Sigma_{\text{ph}}(\omega_n) \\ -\Sigma_{\text{ph}}(\omega_n) & -i\omega_n - \omega_0 - \Sigma_{\text{ph}}(\omega_n) \end{pmatrix}, \quad (\text{A6})$$

with the self-energy given by Eq. (3). In our analysis we focus on the diagonal elements [see Eq. (2)], which describe number-conserving photon processes. The neglect of the off-diagonal components is justified later in this appendix. Performing the summation on the bosonic Matsubara frequencies and the analytic continuation  $i\omega_n \rightarrow \omega + i0^+$ , one obtains the retarded photonic self-energy

$$\begin{aligned} \Sigma_{\text{ph}}^R(\omega) &= \sum_{\mathbf{k}} g^2(\mathbf{k}) \left( \frac{n_F(E_-(\mathbf{k})) - n_F(E_+(\mathbf{k}))}{\omega - (E_+(\mathbf{k}) - E_-(\mathbf{k})) + i0^+} \right. \\ &\quad \left. + \frac{n_F(E_+(\mathbf{k})) - n_F(E_-(\mathbf{k}))}{\omega + (E_+(\mathbf{k}) - E_-(\mathbf{k})) + i0^+} \right), \end{aligned} \quad (\text{A7})$$

with  $n_F(E) = 1/(e^{\beta E} + 1)$  being the Fermi-Dirac distribution. At zero temperature the Fermi factors become step functions,  $n_F(E_{\pm}) = \Theta(\mu - E_{\pm})$ . Pinning the chemical potential at mid-gap ( $\mu = 0$ ) ensures  $E_-(\mathbf{k}) < \mu < E_+(\mathbf{k})$  for every  $\mathbf{k}$ ; hence  $\Theta(\mu - E_-) = 1$  and  $\Theta(\mu - E_+) = 0$ . Consequently, the numerators in Eq. (A7) collapse to the constants  $\pm[n_F(E_-) - n_F(E_+)] = \pm 1$ . Thus the imaginary part of the retarded photonic self-energy  $\Sigma_{\text{ph}}^R$  at zero temperature is given by:

$$\text{Im}[\Sigma_{\text{ph}}^R(\omega)] = -\pi \sum_{\mathbf{k} \in BZ} g^2(\mathbf{k}) [\delta(\omega - \delta E_{\mathbf{k}}) - \delta(\omega + \delta E_{\mathbf{k}})], \quad (\text{A8})$$

having also employed the identity  $\lim_{\epsilon \rightarrow 0} \frac{1}{x+i\epsilon} = \text{P.V.}(\frac{1}{x}) - i\pi\delta(x)$  to isolate the imaginary part. The real and imaginary parts satisfy the Kramers-Kronig identities [40]:

$$\text{Re}[\Sigma_{\text{ph}}^R(\omega)] = \frac{2}{\pi} \text{P.V.} \int_0^{\infty} \frac{\omega' \text{Im}[\Sigma_{\text{ph}}^R(\omega')]}{\omega'^2 - \omega^2} d\omega'. \quad (\text{A9})$$

In the region of frequency we are primarily interested in throughout this work,  $\omega \simeq E_g$ , the sum in (A8) is dominated by states lying close to the band-edge critical point  $\mathbf{k}^*$ , as is shown explicitly for the checkerboard insulator in Section B. Assuming that within this region the coupling changes only weakly, we are allowed to neglect its explicit  $\mathbf{k}$ -dependence [41] and set  $g \equiv g(\mathbf{k}^*) \neq 0$ . Then, the contribution to the imaginary part of the retarded self-energy is determined by the JDOS defined in Eq. (6), as made explicit in Eq. (4). Once  $\Sigma_{\text{ph}}^R(\omega)$  is known, the polaritonic dispersion and spectral width are obtained by solving the secular equation  $\det\{\mathcal{D}_{\text{ph}}^R(\omega)\} = 0$ . However, since the effective action has been truncated at quadratic order in the photon fields, neglecting quartic corrections arising from the effective four-photon interaction vertex [Fig. 8(b)], the resulting dispersions are perturbatively accurate only up to second order in the light-matter coupling  $g$ . One can then also safely neglect the contribution coming from off-diagonal terms in the Nambu structure of Eq. (A6), represented in Fig. 8(a), because it contributes only to fourth order in the coupling. Performing this approximation is equivalent to neglect in the effective action all terms that violate photon-number conservation and to work only with the retarded photonic propagator  $D_{\text{ph}}^R(t) = -i\theta(t) \langle [\hat{a}(t), \hat{a}^\dagger(0)] \rangle$ , as was done in Section III.

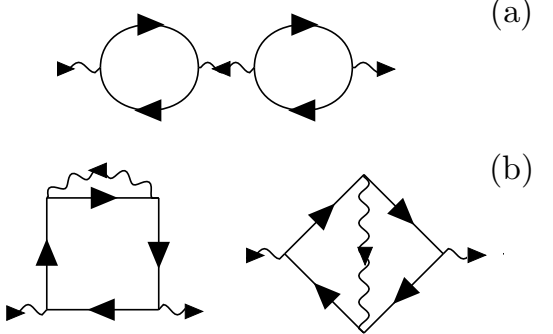


FIG. 8. Neglected corrections to the polaritonic dispersion and spectral width at fourth order in the coupling  $g$ . (a) Contribution of off-diagonal terms in Eq. (A6). (b) Corrections from the effective four-photon vertex interaction.

## Appendix B: Analytical derivation of JDOS for the checkerboard lattice

This appendix presents two complementary analytical routes to derive the singularity in the JDOS of the checkerboard lattice at the gap [see Eq. (7)]. First, we work directly with the exact tight-binding dispersion, arriving at a closed-form expression that is valid across the entire BZ. Second, we focus on the low-energy physics near the M point and employ the Taylor expansion of the bands given in Eq. (13): this highlights the connection

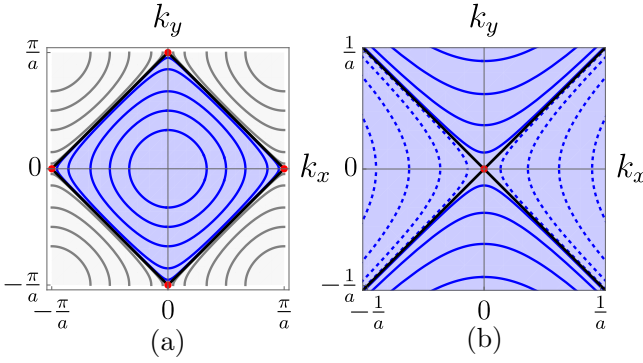


FIG. 9. (a) Constant-energy contours of the NN tight-binding dispersion on a square lattice,  $\varepsilon(k_x, k_y) = -2t [\cos(k_x a) + \cos(k_y a)]$  inside the corresponding first BZ  $\mathcal{Q} = \{|k_x|, |k_y| < \pi/a\}$ . The blue shaded zone is the reduced BZ zone for the checkerboard and red dots indicate the  $M$  point and its images at the four vertices. (b) Constant-energy contours of the Taylor-expanded band-gap dispersion of the checkerboard lattice,  $\delta E(\mathbf{k}) = E_+(\mathbf{k}) - E_-(\mathbf{k})$ , plotted with momenta measured from  $\mathbf{k}^* = (\pi/a, 0)$ . Blue lines correspond to energies  $\delta E_{\mathbf{k}} > E_g$ ; the black line corresponds to the  $\mathbf{k}$ -points exactly at the gap,  $\delta E_{\mathbf{k}} = E_g$ .

between the  $M$  point and the singular behavior displayed in Eq. (7).

### 1. Derivation from the full Tight-Binding Dispersion

For the tight-binding checkerboard lattice introduced in Section IV, the exact band energies are given in Eq. (12). Inserting those dispersions into the definition (6) of the JDOS and taking the continuum limit of the momentum sum yields:

$$J(\omega) = \int_{\mathcal{D}} \frac{d\mathbf{k}}{(2\pi)^2} \delta \left( \omega - 2\sqrt{\varepsilon_{\mathbf{k}}^2 + (E_g/2)^2} \right). \quad (\text{B1})$$

Here,  $\mathcal{D} = \{|k_x| + |k_y| \leq \pi/a\}$  denotes the diamond-shaped reduced BZ, illustrated in Fig. 9(a), inside the full BZ of the square-lattice tight-binding dispersion  $\varepsilon_{\mathbf{k}} = -2t [\cos(k_x a) + \cos(k_y a)]$  in the absence of a staggered potential. For a real function  $F(s)$  with isolated simple zeros  $s_i$ , one has the standard identity

$$\delta(F(\varepsilon)) = \sum_i \frac{\delta(\varepsilon - \varepsilon_i)}{|F'(\varepsilon_i)|}. \quad (\text{B2})$$

Choosing  $F(\varepsilon) = \omega - 2\sqrt{\varepsilon^2 + (E_g/2)^2}$ , the solutions of  $F(\varepsilon) = 0$  are

$$\varepsilon_{\pm} = \pm \sqrt{\omega^2 - E_g^2} / 2 \quad \text{for } \omega \geq E_g, \quad (\text{B3})$$

and the derivatives evaluate to  $F'(\varepsilon_{\pm}) = -\frac{4\varepsilon_{\pm}}{\omega}$ . Applying the identity (B2) to Eq. (B1) yields

$$J(\omega) = \frac{\theta(\omega - E_g) \omega}{2\sqrt{\omega^2 - E_g^2}} \int_{\mathcal{D}} \frac{d\mathbf{k}}{(2\pi)^2} \delta \left( \varepsilon_{\mathbf{k}} + \sqrt{\omega^2 - E_g^2} / 2 \right). \quad (\text{B4})$$

Note that only the contribution from the negative root,  $\varepsilon_- = -\sqrt{\omega^2 - E_g^2}/2$ , survives. This happens because the negative branch energy contours  $\varepsilon = s_-$  [blue curves in Fig. 9(a)] lie entirely inside the diamond  $\mathcal{D}$ , whereas the positive branch energy contours  $\varepsilon = s_+$  [grey curves in Fig. 9(a)] fall outside this region and therefore do not contribute to the integral. Eq. (B4) can then be recast in terms of the square-lattice density of states,

$$\rho_{\varepsilon}(E) = \frac{1}{(2\pi)^2} \int_{\mathcal{Q}} d\mathbf{k} \delta(E - \varepsilon_{\mathbf{k}}), \quad (\text{B5})$$

where  $\mathcal{Q} = \{|k_x|, |k_y| < \pi/a\}$  denotes the full BZ, yielding

$$J(\omega) = \frac{\theta(\omega - E_g) \omega}{2\sqrt{\omega^2 - E_g^2}} \rho_{\varepsilon} \left( -\sqrt{\omega^2 - E_g^2} / 2 \right). \quad (\text{B6})$$

Although Eq. (B5) formally integrates over the entire square BZ, the negative argument  $-\sqrt{\omega^2 - E_g^2}/2$  restricts the support to states lying within the diamond  $\mathcal{D}$ , thereby making Eq. (B6) exactly equivalent to Eq. (B4).

The density of states for a NN tight-binding band on a square lattice is standard textbook material (see Ref. [42] for a derivation) and reads

$$\rho_{\varepsilon}(E) = \frac{1}{2\pi^2 a^2 t} K \left( \sqrt{1 - (E/4t)^2} \right) \theta(4t - |E|), \quad (\text{B7})$$

where  $K$  denotes the complete elliptic integral of the first kind. Inserting Eq. (B7) into the factorized expression Eq. (B6) gives the closed form

$$J(\omega) = \frac{\theta(\omega - E_g) \omega}{4\pi^2 a^2 t \sqrt{\omega^2 - E_g^2}} K \left( \sqrt{1 - \frac{\omega^2 - E_g^2}{64t^2}} \right). \quad (\text{B8})$$

For small energies  $|E| \ll 4t$  one has the expansion

$$K \left( \sqrt{1 - (E/4t)^2} \right) = -\log(|E|/4t) + \mathcal{O}((E/4t)^2), \quad (\text{B9})$$

so that, setting  $E = -\sqrt{\omega^2 - E_g^2}/2$  as dictated by Eq. (B6), one immediately recovers the additional logarithmic divergence of Eq. (7). The logarithmic enhancement is therefore traced back to the conventional 2D VHS associated with the saddle point of the square lattice dispersion  $\varepsilon_{\mathbf{k}}$  at the point  $\mathbf{k}^* = (\pi/a, 0)$  [29].

## 2. Derivation from the Taylor-expanded dispersion around the M point

Inserting the energy bands expanded around the critical point  $\mathbf{k}^*$  given in Eq. (13) into the definition of the JDOS, Eq. (6), yields

$$J(\omega) = \int_{|\mathbf{k}|<\Lambda} \frac{dk_x dk_y}{(2\pi)^2} \delta\left(\omega - E_g - 2\gamma[(k_x a)^2 - (k_y a)^2]^2\right), \quad (\text{B10})$$

where, through the shift  $\mathbf{k} \rightarrow \mathbf{k} - \mathbf{k}^*$ , we have centred the reference frame at  $\mathbf{k}^*$  and introduced a momentum cutoff  $\Lambda$  to model the finite bandwidth. It is convenient to recast the JDOS in the form

$$J(\omega) = \frac{1}{2a^2\gamma} \rho(\tilde{\epsilon}) \Big|_{\tilde{\epsilon}=(\omega-E_g)/(2\gamma)}, \quad (\text{B11})$$

where the dimensionless density of states is defined as

$$\rho(\tilde{\epsilon}) = \int_{|\mathbf{x}|<\tilde{\Lambda}} \frac{dx dy}{(2\pi)^2} \delta(\tilde{\epsilon} - \tilde{\epsilon}(x, y)), \quad (\text{B12})$$

and involves the dimensionless dispersion

$$\tilde{\epsilon}(x, y) = (x^2 - y^2)^2. \quad (\text{B13})$$

Here we introduced the dimensionless variables  $x = k_x a$  and  $y = k_y a$ , together with the dimensionless cutoff  $\tilde{\Lambda} = \Lambda a$  and the dimensionless energy  $\tilde{\epsilon} = \epsilon/(2\gamma)$ . The Dirac delta confines the integration to the constant-energy contour

$$S(\tilde{\epsilon}) = \{(x, y) : \tilde{\epsilon}(x, y) = \tilde{\epsilon}, |x| \leq \tilde{\Lambda}\}, \quad (\text{B14})$$

giving the line integral

$$\rho(\tilde{\epsilon}) = \frac{1}{4\pi^2} \oint_{S(\tilde{\epsilon})} \frac{dl}{|\nabla_{\mathbf{x}} \tilde{\epsilon}|}. \quad (\text{B15})$$

Here  $l$  is the arclength parameter along  $S(\tilde{\epsilon})$ . For  $\tilde{\epsilon}(x, y) = (x^2 - y^2)^2$  the condition  $\tilde{\epsilon}(x, y) = \tilde{\epsilon}$  reduces to  $x^2 - y^2 = \pm \tilde{\epsilon}^{1/2}$ . Hence the full contour decomposes into two branches:

$$S_1(\tilde{\epsilon}) = \left\{ (x, y) : y = \pm \sqrt{x^2 + \tilde{\epsilon}^{1/2}}, |x| \leq \tilde{\Lambda} \right\},$$

$$S_2(\tilde{\epsilon}) = \left\{ (x, y) : y = \pm \sqrt{x^2 - \tilde{\epsilon}^{1/2}}, |x| \geq \tilde{\epsilon}^{1/4}, |x| \leq \tilde{\Lambda} \right\}. \quad (\text{B16})$$

Thus  $S(\tilde{\epsilon}) = S_1(\tilde{\epsilon}) \cup S_2(\tilde{\epsilon})$ . Consequently, the density of states separates into two contributions,

$$\rho(\tilde{\epsilon}) = \rho_1(\tilde{\epsilon}) + \rho_2(\tilde{\epsilon}), \quad \rho_i(\tilde{\epsilon}) = \frac{1}{4\pi^2} \oint_{S_i(\tilde{\epsilon})} \frac{dl}{|\nabla_{\mathbf{x}} \tilde{\epsilon}|} \quad (i = 1, 2).$$

The subset  $S_1$  has two branches with vertices at  $(0, \pm \tilde{\epsilon}^{1/4})$  that open vertically (upward and downward), whereas  $S_2$  has two branches with vertices at  $(\pm \tilde{\epsilon}^{1/4}, 0)$  that open horizontally (leftward and rightward). Fig. 9(b) depicts these contours as solid and

dashed blue lines, respectively. Note that all branches correspond to  $\tilde{\epsilon} > 0$ . In the original variables, they correspond to  $\omega > E_g$ . As  $\tilde{\epsilon}$  approaches zero, the blue contours shrink until, at  $\tilde{\epsilon} = 0$  ( $\omega = E_g$ ), they become two diagonally crossing critical lines (black lines in Fig. 9(b)) intersecting at  $(0, 0)$ , i.e. the point  $\mathbf{k} = \mathbf{k}^*$  in the shifted reference frame. Notice that for  $\tilde{\epsilon} < 0$  no constant-energy contours exist, reflecting the absence of available states below the gap.

Since the dispersion  $\tilde{\epsilon}(x, y) = (x^2 - y^2)^2$  and the integrand  $dl/|\nabla \tilde{\epsilon}|$  are invariant under the exchange  $x \leftrightarrow y$ , which maps  $S_1(\tilde{\epsilon})$  onto  $S_2(\tilde{\epsilon})$ , the two contour integrals are identical,

$$\rho_1(\tilde{\epsilon}) = \rho_2(\tilde{\epsilon}),$$

so it suffices to evaluate only one of the two. We choose  $\rho_1(\tilde{\epsilon})$ . Along the upper branch of  $S_1(\tilde{\epsilon})$  we may write  $y(x) = \sqrt{x^2 + \sqrt{\tilde{\epsilon}}}$  with  $|x| \leq \tilde{\Lambda}$ . The arc-length element is  $dl = \sqrt{1 + (dy/dx)^2} dx = \sqrt{(2x^2 + \sqrt{\tilde{\epsilon}})/(x^2 + \sqrt{\tilde{\epsilon}})} dx$ , whereas on the same contour  $|\nabla \tilde{\epsilon}| = 4\sqrt{\tilde{\epsilon}}\sqrt{2x^2 + \sqrt{\tilde{\epsilon}}}$ . Their ratio therefore becomes

$$\frac{dl}{|\nabla \tilde{\epsilon}|} = \frac{dx}{4\sqrt{\tilde{\epsilon}}\sqrt{x^2 + \sqrt{\tilde{\epsilon}}}}.$$

Because the integrand is even in  $x$  and the lower branch ( $y \rightarrow -y$ ) contributes identically, the integral over the whole subset  $S_1$  gains an overall factor 4. Substituting into the definition, one obtains

$$2\rho_1(\tilde{\epsilon}) = \frac{2}{4\pi^2} \int_{S_1(\tilde{\epsilon})} \frac{dl}{|\nabla \tilde{\epsilon}|} = \frac{2}{4\pi^2\sqrt{\tilde{\epsilon}}} \int_0^{\tilde{\Lambda}} \frac{dx}{\sqrt{x^2 + \sqrt{\tilde{\epsilon}}}},$$

where we note the inverse square-root divergence as  $\tilde{\epsilon} \rightarrow 0$ . The remaining integral is elementary, giving

$$\rho(\tilde{\epsilon}) = 2\rho_1(\tilde{\epsilon}) = \frac{2}{4\pi^2\sqrt{\tilde{\epsilon}}} \operatorname{arcsinh}(\tilde{\Lambda} \tilde{\epsilon}^{-1/4}),$$

For  $\tilde{\epsilon} \rightarrow 0$  this behaves as  $\rho(\tilde{\epsilon}) \simeq \frac{1}{2\pi^2\sqrt{\tilde{\epsilon}}} (-\frac{1}{4} \ln |\tilde{\epsilon}|)$ , thereby making the logarithmic enhancement explicit. Finally restoring the dimensionful JDOS through Eq. (B11) reproduces the behavior shown in Eq. (7).

## Appendix C: Analytical derivation of $\operatorname{Re}[\Sigma_{\text{ph}}^R(\omega)]$ for $\omega \sim E_g^-$

In Fig. 5 we plotted the curves  $\operatorname{Im} \Sigma_{\text{ph}}^R(\omega)$  and  $\operatorname{Re} \Sigma_{\text{ph}}^R(\omega)$  corresponding to three insulating cases: the 1D and 2D parabolic bands, and the checkerboard lattice. We have commented the singular behaviors of both quantities at the band-gap energy  $E_g$  in all three cases. These behaviors are summarized in the first two columns of Table I. We recall that the features observed in  $\operatorname{Im} \Sigma_{\text{ph}}^R(\omega)$  are the same of the JDOS  $J(\omega)$  due to the relation

in Eq. (4). The forms followed by  $\text{Im} \Sigma_{\text{ph}}^R(\omega)$  in the two parabolic cases are standard textbook results [4]. The behavior of  $\text{Im} \Sigma_{\text{ph}}^R(\omega)$  (and of  $J(\omega)$ ) in the checkerboard case, shown in Eq. (7), was already justified in Section B. In this appendix, we derive the behavior of  $\text{Re} \Sigma_{\text{ph}}^R(\omega)$  in the limit  $\omega \rightarrow E_g^-$  for the three cases of Table I. These expressions can be obtained by applying the Kramers-Kronig relation given in Eq. (5), assuming that the function  $J(\omega)$  is known for each case. For a sub-gap frequency  $\omega = (1 - \epsilon)E_g$  with  $\epsilon > 0$ , the pole lies strictly outside the integration domain, so no Cauchy principal value is needed, and we have the expression

$$\text{Re} \Sigma_{\text{ph}}^R(\epsilon) \propto I(\Lambda, \epsilon) \equiv \int_{1+\delta}^{\Lambda} dx \frac{x \tilde{J}(x)}{x^2 - (1 - \epsilon)^2}, \quad (\text{C1})$$

where all the frequency dependence of  $J(\omega)$  has been encoded in the dimensionless function  $\tilde{J}(x)$  and we introduced the dimensionless variable  $x = \omega/E_g$  and a cut-off  $\Lambda$  to model the physical bandwidth limit. The behavior of the integral  $I(\Lambda, \epsilon)$  in (C1) in the limit  $\epsilon \rightarrow 0^+$  can be obtained analytically for each of the three cases.

We first carry out the calculation explicitly for the checkerboard case, for which  $\tilde{J}(x) = \log(x - 1)/\sqrt{x - 1}$ . Making the substitution  $x = 1 + t^2$  ( $dx = 2t dt$ ) with  $t \in [0, \sqrt{\Lambda - 1}]$  removes the square root and casts the integral in the form

$$I_{\text{ch}}(\Lambda, \epsilon) = -2 \int_0^{\sqrt{\Lambda-1}} dt \left( \frac{\log t}{t^2 + \epsilon} + \frac{\log t}{t^2 + 2 - \epsilon} \right). \quad (\text{C2})$$

The only term that can diverge as  $\epsilon \rightarrow 0^+$  is the first one. Because the singularity comes exclusively from the small- $t$  region, we can extend its upper limit to  $\infty$  without changing the leading behavior:

$$I_{\text{ch}}(\Lambda, \epsilon) \xrightarrow{\epsilon \rightarrow 0^+} -2 \int_0^{\infty} dt \frac{\log t}{t^2 + \epsilon} = \frac{\pi}{2} \frac{-\log \epsilon}{\sqrt{\epsilon}}, \quad (\text{C3})$$

where, to obtain the final equality, we introduced the new integration variable  $u = t/\sqrt{\epsilon}$ , recognized the indefinite integral  $\int \frac{du}{1+u^2} = \arctan u$  and employed the identity  $\int_0^{\infty} \frac{\log u}{1+u^2} du = 0$ . To recover the full value of  $I_{\text{ch}}(\Lambda, \epsilon)$  one should subtract the finite “tail”  $\int_{\sqrt{\Lambda-1}}^{\infty} \log t/(t^2 + \epsilon) dt$  that was introduced by extending the upper limit to  $\infty$ , and add the second, always-convergent integral appearing in Eq. (C2). Retaining these pieces yields an additional,  $\Lambda$ -dependent constant that follows the leading term and remains finite as  $\epsilon \rightarrow 0^+$ . Hence

$$I_{\text{ch}}(\Lambda, \epsilon) = \frac{\pi}{2} \frac{-\log \epsilon}{\sqrt{\epsilon}} + \mathcal{O}(1). \quad (\text{C4})$$

For the remaining two cases the calculation proceeds analogously to the checkerboard example. In the parabolic 1D case, where  $\tilde{J}(x) = 1/\sqrt{x - 1}$ , rewriting the integral in terms of the variable  $t$  splits it into two parts:

$$I_{\text{1D}}(\Lambda, \epsilon) = \int_0^{\sqrt{\Lambda-1}} dt \left( \frac{1}{t^2 + \epsilon} + \frac{t^2}{t^2 + \epsilon} \right). \quad (\text{C5})$$

Extending the integration of the first term to  $\infty$  one finds

$$I_{\text{1D}}(\Lambda, \epsilon) = \frac{\pi}{2\sqrt{\epsilon}} + \mathcal{O}(1), \quad (\text{C6})$$

having once again substituted  $t = u\sqrt{\epsilon}$  and recognized the same indefinite integral used in the checkerboard case. Finally, in the parabolic 2D case, for which  $\tilde{J}(x) = 1$ , we have

$$I_{\text{2D}}(\Lambda, \epsilon) = \int_0^{\sqrt{\Lambda-1}} dt \left( \frac{t}{t^2 + \epsilon} + \frac{t^3}{t^2 + \epsilon} \right). \quad (\text{C7})$$

Proceeding as before, after the integration we obtain

$$I_{\text{2D}}(\Lambda, \epsilon) = -\frac{1}{2} \ln(\epsilon) + \mathcal{O}(1), \quad (\text{C8})$$

having recognized the indefinite integral  $\int \frac{t dt}{t^2 + \epsilon} = \frac{1}{2} \ln(t^2 + \epsilon)$ . Upon returning to the original frequency variable  $\omega$ , one recovers the singular behaviors reported in the second column of Table I.

#### Appendix D: Analytical derivation of the polariton shift scaling laws

In this section, we present an analytical derivation of the scaling behavior of the polariton shift  $\delta\omega_{\text{P}} = \omega_0 - \omega_{\text{P}}$  as a function of the dimensionless light-matter coupling strength  $\tilde{g} = g/E_g$  in the weak-coupling regime. These scaling laws  $\delta\omega_p(\tilde{g})$  are presented in Fig. 3 and summarized in the third column of Table I. We obtained these results by solving the equation

$$\text{Re}[\mathcal{D}_{\text{ph}}^R(\omega)]^{-1} = \omega - \omega_0 - \text{Re}[\Sigma_{\text{ph}}^R(\omega)] = 0,$$

with  $\omega_0 = E_g$ , in the limit  $\omega \rightarrow E_g^-$ . In this regime, it is justified to approximate  $\text{Re}[\Sigma_{\text{ph}}^R(\omega)]$  around  $\omega \sim E_g^+$  (see the second column of Table I), leading to the following equations:

$$\delta\tilde{\omega}_{\text{P}} = \tilde{g}^2 a_{\text{1D}} \frac{1}{\sqrt{\delta\tilde{\omega}_{\text{P}}}}, \quad (\text{D1})$$

$$\delta\tilde{\omega}_{\text{P}} = -\tilde{g}^2 a_{\text{2D}} \log \delta\tilde{\omega}_{\text{P}}, \quad (\text{D2})$$

$$\delta\tilde{\omega}_{\text{P}} = -\tilde{g}^2 a_{\text{ch}} \frac{\log \delta\tilde{\omega}_{\text{P}}}{\sqrt{\delta\tilde{\omega}_{\text{P}}}}, \quad (\text{D3})$$

where we introduced the dimensionless polariton shift  $\delta\tilde{\omega}_{\text{P}} \equiv \delta\tilde{\omega}/E_g$  and, for each insulating phase, an overall constant prefactor  $a$  that is independent of the light-matter coupling strength  $g$ . The equation for the 1D case can be solved analytically by inspection. For the remaining two cases, the solutions can be written in terms of the Lambert  $W$  function, defined as the solution of  $W(z) e^{W(z)} = z$ . The resulting expressions are:

$$\delta\tilde{\omega}_{\text{P,1D}} = \tilde{g}^{\frac{4}{3}} a_{\text{1D}}^{\frac{2}{3}}, \quad (\text{D4})$$

$$\delta\tilde{\omega}_{\text{P,2D}} = \tilde{g}^2 W((a_{\text{2D}} \tilde{g}^2)^{-1}) a_{\text{2D}}, \quad (\text{D5})$$

$$\delta\tilde{\omega}_{\text{P,ch}} = \tilde{g}^{\frac{4}{3}} [W((2a_{\text{ch}} \tilde{g}^2/3)^{-1})]^{\frac{2}{3}} (2a_{\text{ch}}/3)^{\frac{2}{3}}, \quad (\text{D6})$$

For weak coupling ( $\tilde{g} \rightarrow 0$ ), the Lambert function satisfies  $W(z) \simeq \ln z - \ln \ln z + \dots$  for  $z \gg 1$ ; using this expansion yields the leading-order scaling behaviors reported in the third column of Table I.

## ACKNOWLEDGMENTS

The authors thank D. Efremov and T. Weitz for insightful discussions.

---

[1] D. N. Basov, A. Asenjo-Garcia, P. J. Schuck, X. Zhu, and A. Rubio, *Nanophotonics* **10**, 549 (2020).

[2] D. E. Chang, V. Vuletić, and M. D. Lukin, *Nature Photonics* **8**, 685 (2014).

[3] M. Razeghi, *Fundamentals of Solid State Engineering*, 3rd ed. (Springer, Cham, 2018).

[4] G. Grosso and G. P. Parravicini, *Solid State Physics*, 2nd ed. (Academic Press, Oxford, 2013).

[5] K. B. Arnardottir, O. Kyriienko, M. E. Portnoi, and I. A. Shelykh, *Physical Review B* **87**, 125408 (2013).

[6] D. V. Efremov, A. Shtyk, A. W. Rost, C. Chamon, A. P. Mackenzie, and J. J. Betouras, *Phys. Rev. Lett.* **123**, 207202 (2019).

[7] N. F. Q. Yuan, H. Isobe, and L. Fu, *Nature Communications* **10**, 5769 (2019).

[8] A. Chandrasekaran, A. Shtyk, J. J. Betouras, and C. Chamon, *Physical Review Research* **2**, 013355 (2020).

[9] L. Classen, A. V. Chubukov, C. Honerkamp, and M. M. Scherer, *Phys. Rev. B* **102**, 125141 (2020).

[10] P. Rosenzweig, H. Karakachian, D. Marchenko, K. Küster, and U. Starke, *Phys. Rev. Lett.* **125**, 176403 (2020).

[11] Y. Hu, X. Wu, B. R. Ortiz, S. Ju, X. Han, J. Ma, N. C. Plumb, M. Radovic, R. Thomale, S. D. Wilson, A. P. Schnyder, and M. Shi, *Nat Commun* **13**, 2220 (2022).

[12] A. M. Seiler, F. R. Geisenhof, F. Winterer, K. Watanabe, T. Taniguchi, T. Xu, F. Zhang, and R. T. Weitz, *Nature* **608**, 298 (2022).

[13] A. Chandrasekaran, L. C. Rhodes, E. A. Morales, C. A. Marques, P. D. C. King, P. Wahl, and J. J. Betouras, *Nat Commun* **15**, 9521 (2024).

[14] L. Classen and J. J. Betouras, *Annual Review of Condensed Matter Physics* **16**, 229 (2025).

[15] F. Mivehvar, F. Piazza, T. Donner, and H. Ritsch, *Advances in Physics* **70**, 1 (2021).

[16] M. Inguscio, W. Ketterle, and C. Salomon, eds., *Proceedings, International School of Physics “Enrico Fermi”, 164th Course, “Ultra-cold Fermi Gases”: Varenna, Italy, June 20–30, 2006*, Vol. 164 (IOS Pr., Amsterdam, 2007).

[17] S. Giorgini, L. P. Pitaevskii, and S. Stringari, *Reviews of Modern Physics* **80**, 1215 (2008).

[18] I. Bloch, J. Dalibard, and W. Zwerger, *Rev. Mod. Phys.* **80**, 885 (2008).

[19] X. Li and W. V. Liu, *Reports on Progress in Physics* **79**, 116401 (2016).

[20] Y. Takahashi, Y. Hayamizu, H. Itoh, M. Yoshita, H. Akiyama, L. N. Pfeiffer, and K. W. West, *Applied Physics Letters* **87**, 223119 (2005).

[21] M. Zamfirescu, A. Kavokin, B. Gil, G. Malpuech, and M. Kaliteevski, *Phys. Rev. B* **65**, 161205 (2002).

[22] J. Shaver and J. Kono, *Laser & Photonics Reviews* **1**, 260 (2007).

[23] M. Rohlfing and S. G. Louie, *Physical Review Letters* **82**, 1959 (1999).

[24] M. Rohlfing and S. G. Louie, *Physical Review B* **62**, 4927 (2000).

[25] S. J. Ubrig, H. Yu, Y. Zhao, M. Gibertini, T. Taniguchi, K. Watanabe, A. Imamoğlu, E. Giannini, and A. F. Morpurgo, *Nature Nanotechnology* **15**, 750 (2020).

[26] L. Degiorgi, B. Alavi, G. Mihály, and G. Grüner, *Physical Review B* **44**, 7808 (1991).

[27] W. Jiang, B. Li, X. Wang, G. Chen, T. Chen, Y. Xiang, W. Xie, Y. Dai, X. Zhu, H. Yang, J. Sun, and H.-H. Wen, *Physical Review B* **101**, 121115 (2020).

[28] Note that this quantity, if a momentum-independent coupling  $g(\mathbf{k}) \equiv g$  is considered, is proportional to the Matsubara frequency representation of the interband polarization bubble  $\Pi^R(t) = -i\theta(t)\langle[\hat{P}(t), \hat{P}^\dagger(0)]\rangle$ , with  $\hat{P}(t) = \sum_k \hat{c}_{-,k}^\dagger(t) \hat{c}_{+,k}(t)$ , computed in the absence of light-matter interaction. This follows from the general relation between the dressed photon propagator and the matter polarization function [43].

[29] L. V. Hove, *Physical Review* **89**, 1189 (1953).

[30] G. Wirth, M. Ölschläger, and A. Hemmerich, *Nature Physics* **7**, 147 (2011).

[31] W. Zwerger, *The BCS–BEC Crossover and the Unitary Fermi Gas*, Lecture Notes in Physics, Vol. 836 (Springer, Berlin, 2012).

[32] W. Zwerger, in *Quantum Matter at Ultralow Temperatures, Proceedings of the International School of Physics “Enrico Fermi”, Course 191, Varenna, 7–15 July 2014*, edited by M. Inguscio, W. Ketterle, S. Stringari, and G. Roati (IOS Press, Amsterdam, 2016) pp. 63–141.

[33] C. Maschler, I. B. Mekhov, and H. Ritsch, *Eur. Phys. J. D* **46**, 545 (2008).

[34] M. Modugno and G. Pettini, *New Journal of Physics* **14**, 055004 (2012).

[35] N. W. Ashcroft and N. D. Mermin, *Solid State Physics* (Holt, Rinehart and Winston, New York, 1976).

[36] F. Piazza, P. Strack, and W. Zwerger, *Annals of Physics* **339**, 135 (2013).

[37] A. Raja, A. Chaves, J. Yu, G. Arefe, H. M. Hill, A. F. Rigosi, T. C. Berkelbach, P. Nagler, C. Schüller, T. Korn, C. Nuckolls, J. Hone, L. E. Brus, T. F. Heinz, D. R. Reichman, and A. Chernikov, *Nat Commun* **8**, 15251 (2017).

[38] D. Tebbe, M. Schütt, K. Watanabe, T. Taniguchi, C. Stampfer, B. Beschoten, and L. Waldecker, *npj 2D Mater Appl* **7**, 29 (2023).

[39] I. Carusotto and C. Ciuti, *Rev. Mod. Phys.* **85**, 299 (2013).

[40] A. L. Fetter and J. D. Walecka, *Quantum Theory of Many-Particle Systems* (McGraw-Hill, Boston, 1971).

[41] F. Bassani and G. P. Parravicini, Electronic states and optical transitions in solids, in *International Series of Monographs in the Science of the Solid State*, Vol. 8 (Pergamon Press, Oxford, 1975) Chap. 5.

[42] E. N. Economou, *Green’s Functions in Quantum Physics*, 3rd ed. (Springer, Berlin, 2006).

[43] I. Amelio, L. Korosec, I. Carusotto, and G. Mazza, [Physical Review B \*\*104\*\*, 235120 \(2021\)](#).